Title

Fracture Propagation, Fluid Flow, and Geomechanics of Water-Based Hydraulic Fracturing in Shale Gas Systems and Electromagnetic Geophysical Monitoring of Fluid Migration

Authors

Kim, Jihoon
Um, Evan
Moridis, George

Publication Date

2014-02-04

Fracture Propagation, Fluid Flow, and Geomechanics of Water-Based Hydraulic Fracturing in Shale Gas Systems and Electromagnetic Geophysical Monitoring of Fluid Migration

Jihoon Kim, Evan Schankee Um, and George J. Moridis
Earth Sciences Division, Lawrence Berkeley National Laboratory

This paper, number SPE 168578, was presented at the SPE Hydraulic Fracturing Technology Conference held in The Woodlands, Texas, USA, 4–6 February 2014.

Abstract

We investigate fracture propagation induced by hydraulic fracturing with water injection, using numerical simulation. For rigorous, full 3D modeling, we employ a numerical method that can model failure resulting from tensile and shear stresses, dynamic nonlinear permeability, leak-off in all directions, and thermo-poro-mechanical effects with the double porosity approach. Our numerical results indicate that fracture propagation is not the same as propagation of the water front, because fracturing is governed by geomechanics, whereas water saturation is determined by fluid flow. At early times, the water saturation front is almost identical to the fracture tip, suggesting that the fracture is mostly filled with injected water. However, at late times, advance of the water front is retarded compared to fracture propagation, yielding a significant gap between the water front and the fracture top, which is filled with reservoir gas. We also find considerable leak-off of water to the reservoir. The inconsistency between the fracture volume and the volume of injected water cannot properly calcuate the fracture length, when it is estimated based on the simple assumption that the fracture is fully saturated with injected water. As an example of flow-geomechanical responses, we identify pressure fluctuation under constant water injection, because hydraulic fracturing is itself a set of many failure processes, in which pressure consistently drops when failure occurs, but fluctuation decreases as the fracture length grows.

We also study application of electromagnetic (EM) geophysical methods, because these methods are highly sensitive to changes in porosity and pore-fluid properties due to water injection into gas reservoirs. Employing a 3D finite-element EM geophysical simulator, we evaluate the sensitivity of the crosswell EM method for monitoring fluid movements in shaly reservoirs. For this sensitivity evaluation, reservoir models are generated through the coupled flow-geomechanical simulator and are transformed via a rock-physics model into electrical conductivity models. It is shown that anomalous conductivity distribution in the resulting models is closely related to injected water saturation, but not closely related to newly created unsaturated fractures. Our numerical modeling experiments demonstrate that the crosswell EM method can be highly sensitive to conductivity changes that directly indicate the migration pathways of the injected fluid. Accordingly, the EM method can serve as an effective monitoring tool for distribution of injected fluids (i.e., migration pathways) during hydraulic fracturing operations.

Introduction

Hydraulic fracturing with multiple horizontal wells has been widely used in stimulating abundant shale gas reservoirs, in order to increase reservoir permeability and productivity (Zoback 2007; Fjear et. al. 2008; Fisher and Warpinski 2012; Zoback et. al. 2010; Cipolla et. al. 2010). Creation of fractures increases the permeability of geological formations by several orders, which can make gas production from very low-permeable reservoirs—such as tight gas and shale gas reservoirs—economically feasible. After the recent success in developing the Barnett shale, other shale gas reservoirs, such as the Marcellus, Eagle Ford, Haynesville, New Albany, Antrim, and Fayetteville shales in the United States, have been considered

as potential resources in the near future. Massive hydraulic fracturing with multiple stage stimulation can significantly enhance reservoir permeability, followed by productivity and increased stimulated rock volume (SRV) (Kargbo et. al. 2010; Arthur et al. 2008).

Environmental scientists have raised a number of issues related to the environmental impact of hydraulic fracturing, including unstable growth of fractures, groundwater contamination, and induced seismicity from fault activation. For example, Osborn et al. (2011) claimed from isotope analysis that methane dissolved in groundwater originated from shale gas reservoirs. Geomechanical failure along the well casing due to incomplete cementing could also be a problem, in that it would create a potential pathway for methane from reservoirs to drinking water aquifers (Zoback et al. 2010). Reservoir engineers, however, argue that the environmental impact of such activity is still limited. For example, according to Fisher and Warpinski (2012), fracture lengths based on measured microseismic data are finite, and fracture tips are far below drinking-water zones. Also, Rutqvist et al. (2013) in their recent study of induced seismicity using numerical simulation showed that the intensity of induced seismicity caused by fault activation is far below the level discernible by humans.

Much research in simulating fracture propagation has been performed on hydraulic fracturing for several decades, in order to estimate SRV and the lengths of the created fractures, mainly based on 2D or pseudo 3D (Perkins and Kern, 1961; Nordren, 1972; Adachi et.al., 2007) . Even though such models can provide numerical efficiency and reduce computational cost, full coupling in 3D between flow and geomechanics is required for rigorous modeling of fracture propagation and more reliable risk assessment. Recently, Ji et al. (2009) and Dean and Schmidt (2009) performed numerical modeling of full 3D hydraulic fracturing in the context of coupled flow and geomechanics. Furthermore, Kim and Moridis (2013) incorporated the double porosity approach as well as simultaneous tensile and shear failure.

Hydraulic fracturing is typically based on water injection, in which water is mixed with some proppants and additional chemicals (King, 2012). Water can easily be accessible and pressurized. However, after hydraulic fracturing operations, it is difficult to withdraw the injected water, which might cause a significant decrease in productivity or increase in adverse chemical reactions (Page and Miskimins 2009; Ribeiro and Sarma 2013). Thus, it is critically important to accurately estimate fracture propagation as well as fluid flow and proppant migration.

In this paper, we numerically investigate fracture propagation by water injection for hydraulic fracturing operations, focusing on fracture propagation and water movement. Note that fracture propagation might not be the same as propagation of the water front, because fracturing is governed by geomechanics, whereas water saturation is determined by fluid flow. The inconsistency between the fracture volume and the injected-water volume means that we cannot properly estimate the dimension of the fracture by simply assuming the fracture to be fully saturated with water. For full 3D rigorous modeling, we employ a numerical method, demonstrated in Kim and Moridis (2013), which can model tensile failure due to normal and shear stresses, dynamic nonlinear permeability and geomechanical moduli, leak-off in all directions during hydraulic fracturing, and thermo-poro-mechanical effects.

Along with the modeling of fracture propagation and fluid flow, it is also important to develop and evaluate geophysical methods for monitoring the migration pathways of injected fluids. Microseismic methods have been widely used in the past decade for estimation of fracture propagation and geometry (e.g. Warpinski et al., 2005; Vermylen and Zoback, 2011). In some cases, however, the magnitudes of microearthquakes have been too small to be reliably recorded in practice. In addition, the microseismic inversion for determining fracture length and width depends strongly on an initial velocity model, and can result in significant ambiguity in hydraulic fracture characterization (Johnston and Shrallow, 2011). To reduce the ambiguity in the microseismic monitoring, we can consider electromagnetic (EM) geophysical methods. When hydraulic fracturing operations force a mixture of fluids and proppant into the formation under high pressure, they generate highly localized changes in porosity and pore fluids. Because EM methods are sensitive to porosity, fluid saturation, and the chemistry of the fluid in pore spaces, they are a promising tool for illuminating migration pathways taken by the injected fluids and proppant, and can complement microseismic methods. In this paper, we investigate the sensitivity of an EM geophysical method to electrical conductivity changes that are directly correlated with hydraulic fracturing operations.

Accordingly, this paper consists of two major parts: coupled flow-geomechanical modeling and EM geophysical modeling. The remainder of this paper is organized as follows: First, we briefly describe a T+M coupled flow-geomechanical modeling algorithm, and then simulate fracture propagation and coupled flow-thermal-geomechanical processes in a tight shale gas reservoir. From this simulation, we also obtain changes in reservoir porosity and permeability, pressure and saturation of gas and water, and fracture openings and displacement over the domain. The resulting reservoir parameters are employed to construct a series of realistic 3D electrical conductivity models using a rock physics model. Subsequently, we evaluate the sensitivity of an EM geophysical method to conductivity changes due to hydraulic fracturing operations. We demonstrate that by using electriomagnetically engineered high-conductivity fluids, we can significantly improve the sensitivity of the EM method to injection-fluid migration pathways.

Hydraulic Fracturing Simulation

Water injection

Two-phase flow within a fracture occurs during water injection of hydraulic fracturing processes. As water flows through the fracture, reservoir gas is pressurized, while some of the water leaks off into the reservoir formation, as shown Fig. 1. In the left part of the figure, a stimulated zone is shown, which consists of a main fracture, several fissures, and partially continuous small fractures, depending on the complexity of the hydraulic fractures (Fisher and Warpinski, 2012). In this way, we can

model the flow and geomechanics of different fractures, using the dual continuum (also called double porosity) approach.

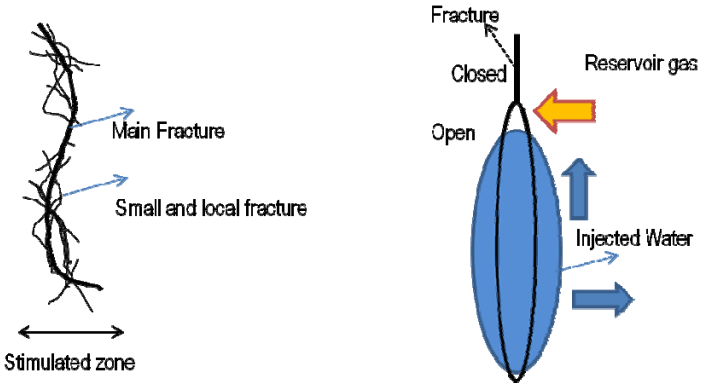

Fig. 1. Schematics of complex fractures and fluid movement around the fractures. Hydraulic fractures create different types of the stimulated zone shown in the left figure. In the right figure, multiphase flow depends on viscous force, buoyancy, and poromechanical effects, opening and closing the fractures.

Let us consider the time when fracturing occurs, when there is little pressure diffusion. At this time scale, after fracturing, pore pressure is still below that required to open the created fracture. We can then assume that reservoir gas fills the fracture space immediately once fracturing occurs, based on the high mobility of gas (i.e., low viscosity and high relative permeability), shown in Fig. 1 (right). When a fracture is closed, water cannot move to the newly created fracture. After the fracture opens, reservoir gas and injected water flow into the new fracture space, by viscous force as well as buoyancy. Furthermore, the increase in the fracture volume can cause a decrease in pore pressure because of poro-mechanical effects, which might allow the reservoir gas to leak into the fracture, again, if the pore pressure is below the gas pressure of the reservoir.

Consider a case in which reservoir pressure and temperature are 17.1 MPa and 58.8°C, respectively. These values come from a generalized model of Marcellus shale. Viscosities for liquid water and gas phases are $4.79\times10^{-4}\,\mathrm{Pa\cdot s}$ and $1.78\times10^{-5}\,\mathrm{Pa\cdot s}$, respectively. Gas density under reservoir conditions, $1.15\times10^{2}\,\mathrm{kg\cdot m^{-3}}$, also cannot be neglected, compared with the density of water, $9.89\times10^{2}\,\mathrm{kg\cdot m^{-3}}$. From the densities and viscosities of water and gas, we can estimate the pattern of water-saturation movement, constructing the following equation for the fractional flow curve, f_w, after ignoring the gradient of capillary pressure within a fracture.

$$f_w = \frac{1 - N_g k_{r,g}}{1 + \dfrac{k_{r,g}}{\mu_g}\dfrac{k_{r,w}}{\mu_w}}, \quad k_{r,J} = \max\left\{0, \min\left\{\left(\frac{S_J - S_{r,J}}{1.0 - S_{r,w}}\right)^{n_k}, 1\right\}\right\}, \tag{1}$$

where N_g, $k_{r,J}$, and μ_J are the gravity number, relative permeability and viscosity of phase *J*, respectively. Subscripts *g* and *w* indicate gas and water phases, respectively. S_J and $S_{r,J}$ are, respectively, saturation and residual (irreducible) saturation of phase *J*. Here we use the modified versions of Stone's relative permeability model.

Fig. 2 shows the fractional flow curves with various gravity numbers. From Fig. 2, we see that the movement of water saturation is likely to be piston-like displacement, generating a shock wave. On the other hand, an aperture distribution along the fracture is continuous. Reservoir gas would then be accumulated within the upper area of the fracture, which yields a *dry zone.* We then anticipate that the gas volume within the fracture would become larger as the simulated zone becomes larger, because reservoir gas that fills the simulated zone moves upward due to buoyancy. Another important issue is how much water infiltrates into the reservoir rock matrix, because leak-off of water into the rock matrix can significantly affect the mobility of gas when gas is produced, reducing relative permeability. Thus, the modeling that can simulate coupled flow and geomechanics is required to accurately predict physical processes during hydraulic fracturing operations.

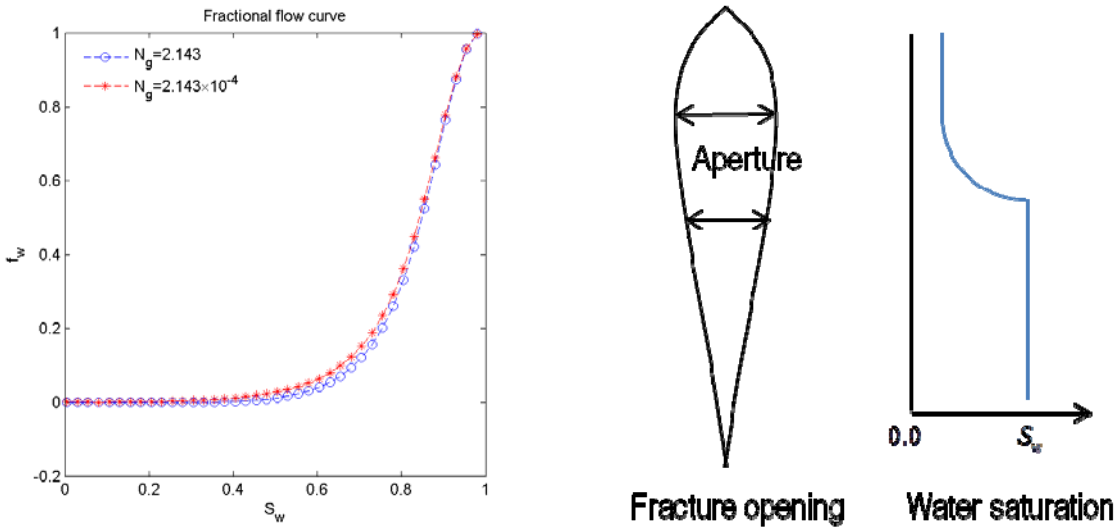

Fig. 2. Left: fractional flow curves at different gravity numbers. Right: Schematics of the fracture opening and water saturation distribution.

Failure condition and permeability

Hydraulic fracturing is based on tensile failure, which creates a fracture and then opens it. We employ a stress-based failure condition for large-scale fracture propagation, rather than a toughness-based condition. According to Chapter 4 in Zoback (2007), once a fracture reaches a sufficient length (e.g., above a few tens of centimeters), the fracture propagates regardless of the rock's fracture toughness. Tensile effective stress at failure is almost constant beyond 1.0m of the fracture length. A toughness-based failure condition is more relevant in small scale-fracture propagation, but might be irrelevant for large-scale fracture propagation (Adachi et al. [2007]). Then, we use a failure condition (Ruiz et al., 2000), written as

$$\sigma'_c \left(= \sqrt{\beta^{-2}\left(t'^2_t + t'^2_s\right) + t'^2_n} \right) \geq T_c, \tag{2}$$

where σ'_c is the effective stress for tensile failure, which consists of shear and normal effective stresses. t'_n, t'_t and t'_s are normal and shear effective stresses acting on a plane (Fig. 3), and T_c is tensile strength. Using β of Eq. 2, we account for the contribution of shear effective stress to tensile failure.

When implementing the tensile failure, we implicitly employ a node-splitting scheme, as shown in Fig. 3 (left). Then, considering vertical fracture propagation, we can simplify the node-splitting scheme into a method that updates outer boundary conditions (i.e., from the Dirichlet condition to the Neumann condition, as shown in Fig. 3 (right)), not introducing an internal boundary (this scheme was previously used in Ji et al. (2009)). We then can reduce computational resources and code management effort.

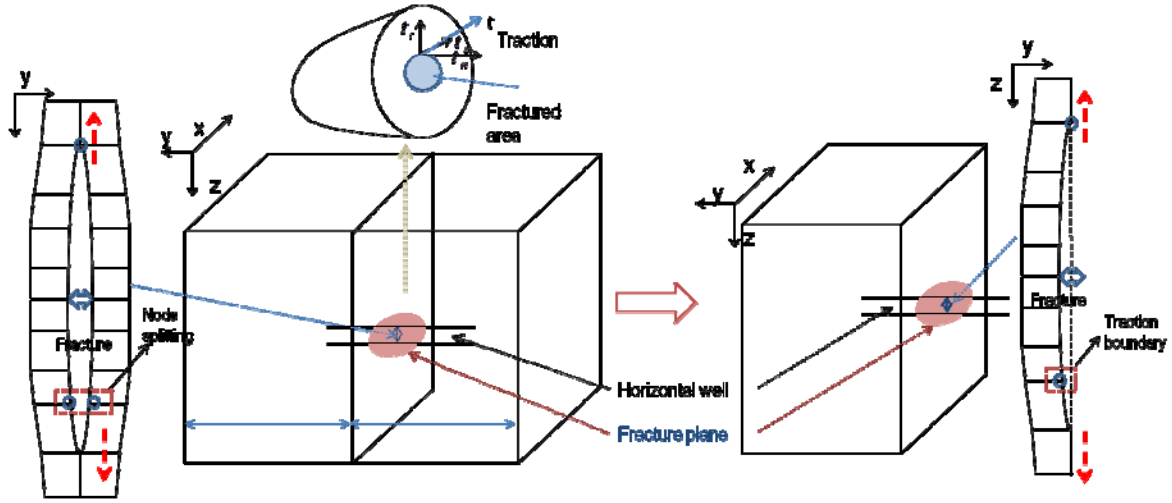

Fig. 3 Schematics of tensile failure in 3D. Left: planar fracture propagation along the vertical direction. Right: modeling of vertical fracture propagation using no horizontal displacement condition at the plane that contains the vertical fracture (Kim and Moridis ,2013).

For the modeling of the fracture permeability corresponding to tensile failure, we use the modified cubic law (e.g., Snow, 1965; Rutqvist and Stephansson, 2003), written as

$$Q_w = a_c \frac{\omega_f^{n_p}}{12\mu_w} H\left(\nabla p - \rho_w \mathbf{g}\right), \tag{3}$$

where ω_f is the aperture, also called fracture opening. Q_w is flow rate of water, H is the fracture plate width, and **g** is the gravity vector. For $n_p = 3.0$, Eq. 3 reduces to the original cubic law. a_c is the correction factor that reflects the fracture roughness. We use a minimum fracture permeability, still much higher than the permeability of intact rock, even when the fracture is closed.

Coupled flow and geomechanics

We employ quasi-static mechanics, based on momentum balance, when solving geological deformation and failure. Governing equations of fluid and heat flow derive from conservation laws of fluid mass and energy. In hydraulic fracturing operations, flow and geomechanics are tightly coupled, because permeability is a strong function of material failure and deformation of a fracture, as described in Eq. (3). The high deformability of fractures also affects coupling in pore volume, which cannot be neglected; this coupling can be modeled by poromechanics (Coussy, 2004). Specifically, according to Berryman (2002) and Kim et al. (2012), porosity coupling using a multiple continuum approach, which can represent a fracture-rock matrix system (or a system of the main fracture and small local fractures), can be modeled as

$$\delta\Phi_l = \left(\frac{\alpha_l^2}{K_l} + \frac{\alpha_l - \Phi_l}{K_s}\right)\delta p_l + 3\alpha_{T,l}\alpha_l \delta T_l - \frac{b_l}{\eta_l}\delta\sigma_v, \quad b_l = -\frac{\alpha_l \eta_l}{K_l}, \tag{4}$$

where Φ is the Lagrange porosity, defined as the ratio of the pore volume in the deformed configuration to the bulk volume in the reference (initial) configuration. The subscription l indicates subelements in a gridblock. T is temperature. K_l, K_s, η_l, $\alpha_{T,l}$, α_l are the drained bulk modulus, intrinsic solid grain modulus, the volume fraction, the thermal dilation coefficient, and Biot's coefficient for subelement l within a gridblock, respectively. σ_v is total mean (volumetric) stress at the gridblock. Then, once fracturing occurs, a single continuum is changed to dual continua that have the main fracture and the damaged zone, having different permeability and porosity during simulation (Fig. 4).

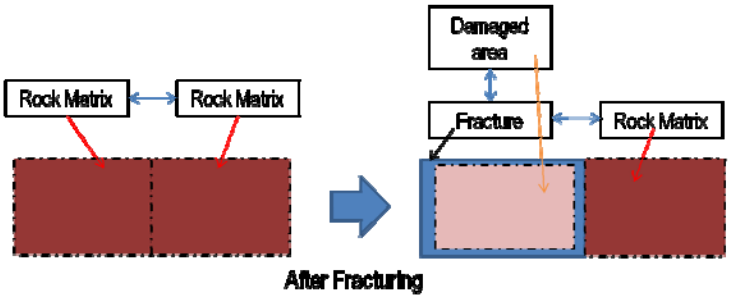

Fig. 4 A schematic of connectivity of the dynamic dual continuum approach. When tensile failure occurs, a single continuum is changed to dual continua that consist of the main fracture and the damaged zone.

In numerical modeling, we employ the finite volume method for flow, in which flow variables take piecewise-constant interpolation. For geomechanics, we use the finite element method, taking linear interpolation of displacement. In time discretization, we employ the backward Euler method. (These discretizations for flow and geomechanics are widely used in reservoir simulation and computational geomechanics communities, respectively.)

We employ a sequential method to solve coupled flow and geomechanics problems. Specifically, we use the fixed-stress sequential method in solving two-way coupling in pore-volume, written as (Kim et al., 2012)

$$\Phi_l^{n+1} - \Phi_l^n = \underbrace{\left(\frac{\alpha_l^2}{K_l} + \frac{\alpha_l - \Phi_l^n}{K_s} \right)}_{\Phi_l^n c_p} \left(p_l^{n+1} - p_l^n \right) + \underbrace{3\alpha_{T,l}\alpha_l}_{\Phi_l^n c_T} \left(T_l^{n+1} - T_l^n \right) - \underbrace{\frac{b_l}{\eta_l} \left(\sigma_v^n - \sigma_v^{n-1} \right)}_{\Delta\Phi_l^n}, \quad (5)$$

where the superscript n is the time level in time discretization. c_p and c_T correspond to the pore compressibility and thermal expansivity used in reservoir simulation, respectively. $\Delta\Phi_l^n$ is called porosity correction, calculated from the previous geomechanics solutions, in order to capture poromechanical effects.

Permeability is calculated based on explicit treatment, depending on failure status and aperture of the fracture at the previous time step. Permeability is a strong function of geomechanical failure, and thus, for further accuracy, we take a small time-step size that ensures no fracturing between two fracturing events.

From the given numerical schemes, we can make use of existing flow and geomechanics codes by constructing an interface between them. In this study, we couple TOUGH+RealGasH2O, a flow simulator, to ROCMECH, a geomechanics simulator, naming the coupled simulator T+M. T+M carries out several verification tests for thermo-poro-mechanics (e.g., the Terzaghi, Mandel, and McNamee-Gibson problems), the opening of static fractures, and fracture propagations for viscosity and toughness-dominated systems, matching the analytical solutions (e.g., Kim and Moridis (2013)).

Simulation domain

Assuming a 3D simulation domain, as shown in Fig.5, we discretize the domain for geomechanics with 50, 5, and 50 gridblocks in x, y, and z directions, respectively. The direction of the minimum compressive principal total stress is perpendicular to the x-z plane. Gridblock sizes in the x and z direction are uniform, i.e., $\Delta x = \Delta z = 3m$. The sizes of the gridblocks in the y direction are non-uniform, i.e., 0.1 m, 0.5 m, 3.0 m, 10.0 m, and 20.0 m. We take 12 G Pa of Young's modulus, E, and 0.3 of Poisson's ratio, ν, respectively. The tensile strength of shale for the reference case is $T_c = 10MPa$. We assume $\beta = 1.0$ for contribution of effective shear stress to tensile failure, identical to the condition of Asahina et al. (2011).

For flow, we share the same discretized domain of geomechanics, having 50, 6, and 50 gridblocks in x, y, and z directions, respectively, with an additional layer in the y direction The additional layer, the thickness of which is 1.0 m, represents half of the width of the stimulated reservoir zone shown in Fig. 1. We assume water to be injected at (x=75 m , z=-1440 m), which is an initial fractured node. We take $8.645 \times 10^{-18} m^2$ for the intrinsic permeability of the rock matrix, where 1 darcy is $9.87 \times 10^{-13} m^2$. For relative permeability, we use $S_{r,w} = 0.08$ and $S_{r,g} = 0.01$. In addition, $n_p = 3.0$ and $a_c = 0.14$ are set for the modified cubic law. Biot's coefficient, α, is 1.0, and the thermal dilation coefficient is $\alpha_T = 4.5 \times 10^{-5}\,^{\circ}\mathrm{C}^{-1}$. We apply the dual continuum approach to the simulated zone, consisting of the main fracture and the damaged zone, which includes small local fractures. The permeability of the main fracture, k_f^p, is calculated from Eq. (3); the permeability of the damaged zone, k_m^p, is calculated from $k_m^p = \chi^m k_f^p$, where $\chi^m = 10^{-3}$. The lower limit of k_p^f is 60 mD. For Eq. (5), we assume $K_l = 500MPa$ for both continua. We set $\eta_f = 0.01$ and $\eta_m = 0.99$.

For the initial conditions, reservoir pressure is initially set at 17.10 MPa at 1350 m depth, with a 12.44 kPa/m gradient. Initial temperature is 58.75°C at 1350 m in depth, with a 0.025°C /m gradient. Based on estimation of the generic total stress distribution (Zhang and Stephansson, 2010), the initial total principal stresses are -36.40MPa, -23.30MPa, and -29.12MPa at 1350 m depth in x, y, and z directions, respectively, where tensile stress is positive. The corresponding stress gradients are -27.0kPa/m, -17.59kPa/m, and -21.57kPa/m, respectively. The injection rate is 40 kg/s at the injection point, with no-flow boundary conditions for flow. For geomechanics, there are no-horizontal-displacement boundary conditions for the sides, except for the fracture nodes, with no displacement boundary at the bottom. We also assume gravity and bulk density to be 2200 kg/m^3.

For capillarity, we use the van Genuchten capillary pressure model (Genuchten, 1980), written as

$$P_c = \Pi_c \left(\left(\frac{S_w - S_{r,w}}{1 - S_{r,g} - S_{r,w}} \right)^{-\frac{1}{\lambda_p}} - 1 \right)^{1-\lambda_p}, \quad (6)$$

where P_c, λ_p, and Π_c are capillary pressure, the exponent that characterizes the capillary pressure curve, and the capillary modulus, respectively. $\lambda_p = 0.45$ and $\Pi_c = 20kPa$ in Eq. 6. $S_{r,w} = 0.05$ and $S_{r,g} = 0.0$ are used for capillarity, which are slightly smaller values than those used in the relative permeability model, in order to prevent unphysical behavior (Moridis et al., 2008).

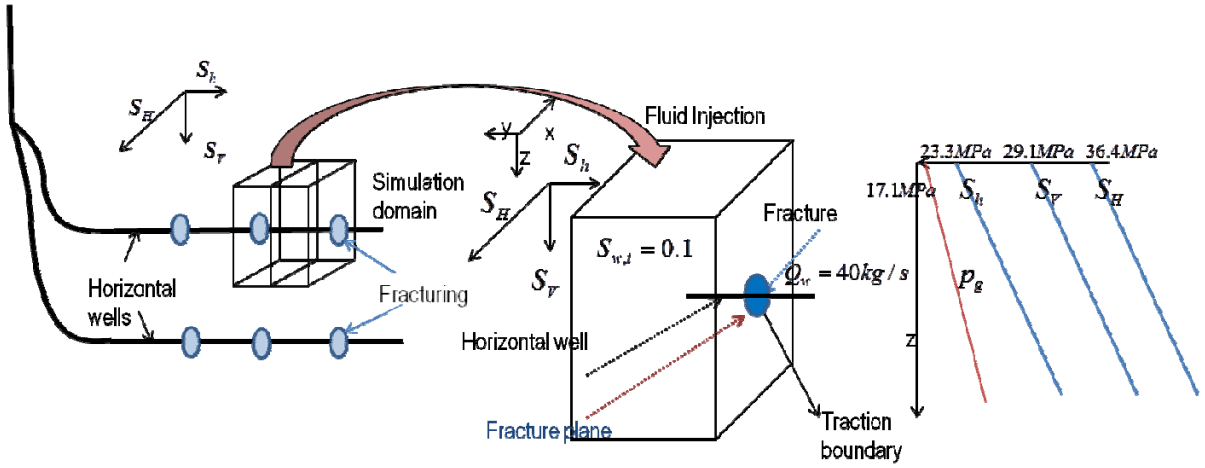

Fig. 5. A domain of hydraulic fracturing simulation in 3D. We assume a simultaneous fracturing operation, where the horizontal wells are aligned with the direction of the minimum compressive principal total stress, S_h.

Numerical results

Fig. 6 shows fracture propagation and fracture opening for the main fracture at different times. Because of the point source for water injection, the fracture propagates in an elliptic shape, as shown in the left-hand part of the figure. As shown in the right-hand part of the figure, the aperture of the fracture is continuous when the fracture is open. The fracture propagation is stable, which means that it depends on the injection time, and that it can be controlled by the injection rate and time.

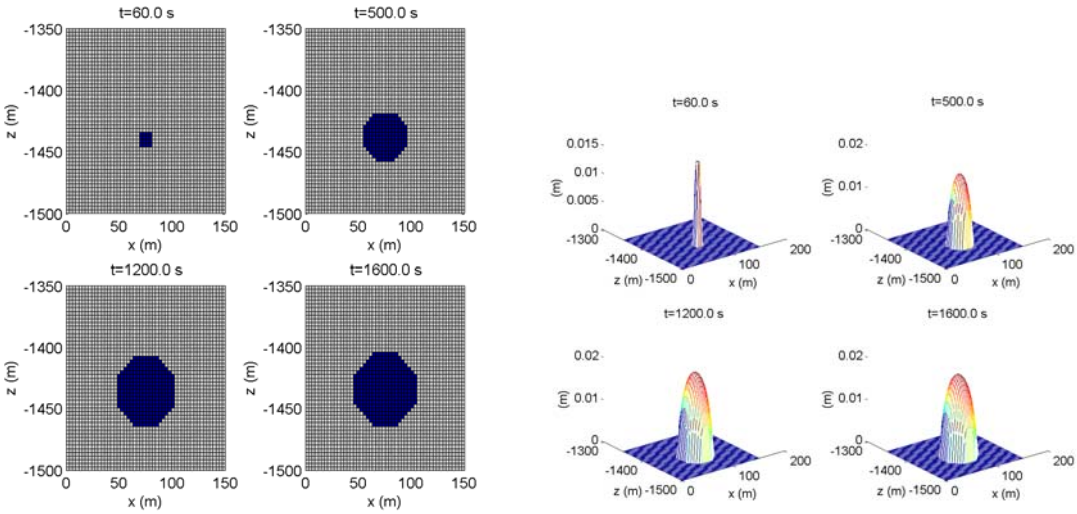

Fig. 6 Left: growth of the fracture induced by water injection. Right: the corresponding fracture opening. The fracture propagation depends on the injection time.

Fig. 7 shows flow and geomechanical responses at different monitoring points. Due to the discontinuity of fracturing events in time (Fig. 7(a)), we identify pressure fluctuation under the constant rate of water injection, observing that pressure drops each time that failure occurs (Fig. 7(b)). Pressure fluctuation is much more severe at early times than at late times, because at early times the fracture volume is small, and pressure responses of incompressible fluid are more sensitive to smaller fractured areas. Then, the fluctuation decreases as the fracture length grows, because the fractured area becomes large. (This pressure oscillation can also be found in Tzchichholz and Herrmann [1995]). Along with the pressure fluctuation, the aperture of the fracture exhibits the same behavior as does pressure (Fig. 7(c)). For displacement, we observe the uplift at the top of the simulation domain, owing to expansion of the domain induced by fluid injection (Fig. 7(d)).

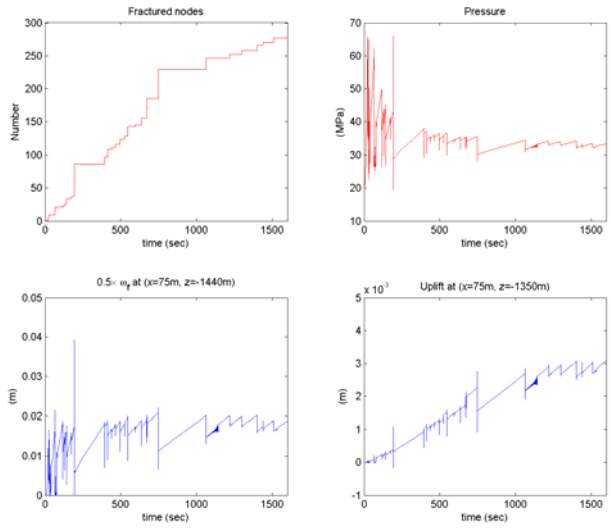

Fig. 7 Evolution of geomechanics and flow variables: (a) number of fractured nodes, (b) pressure at the injection point , (c) aperture of the fracture at the injection point, (d) displacement at (x=75m, z=-1350m). Fracturing events are discontinuous, which results in fluctuation in pressure and the aperture. The oscillation is more dominant at early times due to small volume of the fracture.

In Fig. 8, we find the existence of reservoir gas within the fracture. In particular, we identify a large amount of gas within the fracture at late times. As the fracture grows, reservoir gas initially captured in the stimulated zone moves upward due to buoyancy, occcupying the upper part of the fracture, while the injected water fills the lower part of the fracture because of gravity. In Fig. 9, we also find that, at early times, the water saturation front is almost identical to the fracture tip, indicating that the fracture is mostly filled with injected water. However, at late times, the water front's advance is retarded compared to the fracture propagation, yielding a significant gap between the water front and the fracture top, which is filled with reservoir gas. As stated above, fracture propagation is not the same as water-front propagation, because fracturing is governed by geomechanics, whereas water saturation is determined by fluid flow. We thus cannot assume the fracture to be fully saturated with injected water when estimating the dimensions of the fracture.

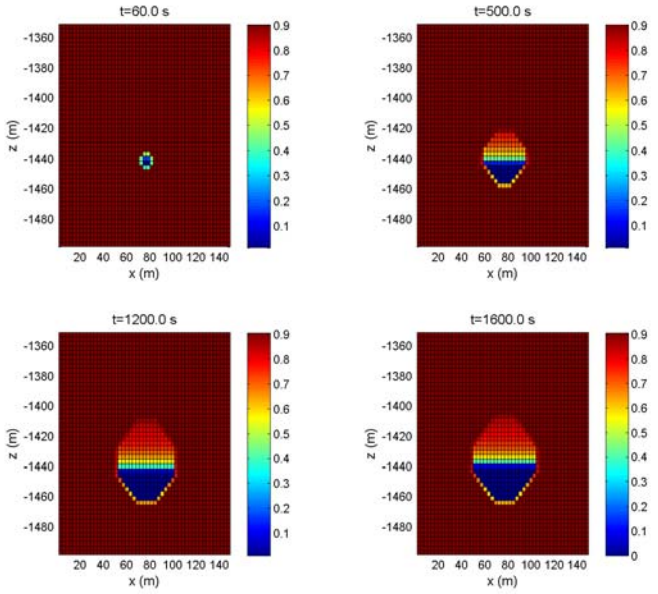

Fig. 8 Gas saturation at different times. The color-bar indicates gas saturation. Gas is accumulated at the upper part of the fracture, while water fills the lower part.

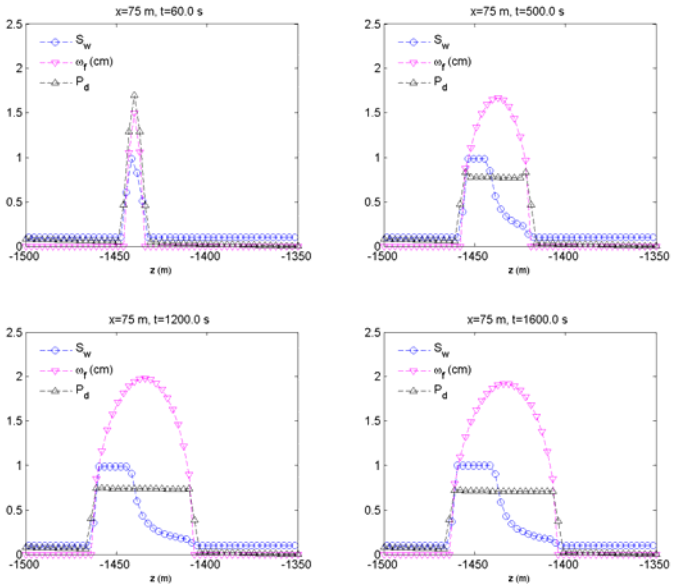

Fig. 9 Distributions of water saturation, aperture, dimensionless pressure (p_d) at x=75m. $p_d = \frac{p - p_L}{p_U - p_L}$, **where p_U=40MPa and P_L=17.1MPa. The aperture is continuous along the fracture, while gas saturation is somewhat discontinuous. At early times, water fills almost all parts of the fracture, whereas gas takes up a considerable volume within the fracture at late times.**

In Fig. 10, we find considerable leak-off of water to the reservoir. Gas saturations within the damaged zone and intact reservoir nearest to the stimulated zone are significantly low, indicating that a considerable amount of water has infiltrated into the reservoir. When the leak-off of water cannot be stopped, it might potentially reduce gas production.

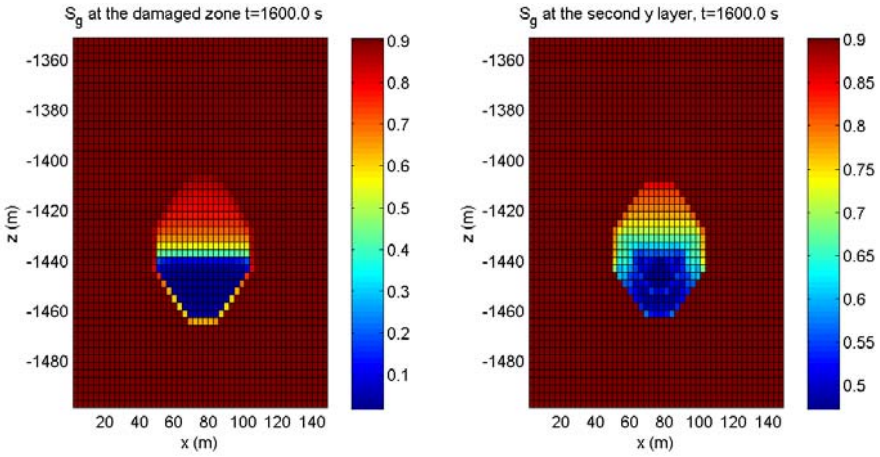

Fig. 10 Distribution of gas saturations at the damaged zone (left figure) and the rock matrix (right figure). The large amount of water infiltrates from the fracture into the reservoir.

Electromagnetic Monitoring of Fluid Migration Pathways

Finite element solution to Maxwell's equations for electromagnetic modeling

EM geophysical responses to an Earth model are governed by solving Maxwell's equations. Maxwell's equations in the frequency domain are given by

$$\nabla \times \mathbf{e}(\mathbf{r}) = -\hat{i}\omega \mathbf{b}(\mathbf{r}), \tag{7}$$

$$\mu_o^{-1} \nabla \times \mathbf{b}(\mathbf{r}) = \sigma(\mathbf{r})\mathbf{e}(\mathbf{r}) + \hat{i}\varepsilon_o \omega \mathbf{e}(\mathbf{r}) + \mathbf{J}_s(\mathbf{r}), \tag{8}$$

$$\nabla \cdot \mathbf{e}(\mathbf{r}) = \rho_v \varepsilon_o^{-1}, \tag{9}$$

$$\nabla \cdot \mathbf{b}(\mathbf{r}) = 0, \tag{10}$$

where $\mathbf{e}(\mathbf{r})$ is the electric field at position $\mathbf{r}$, $\mathbf{J}_s(\mathbf{r})$ is an electric current source at angular frequency ω, μ_o is the magnetic permeability, $\sigma(\mathbf{r})$ is the electrical conductivity at position $\mathbf{r}$, ε_o is the dielectric permittivity, and ρ_v is the electric charge density. In this paper, μ_o within the earth and air is assumed to be constant and is set to that of free space ($4\pi \times 10^{-7}$ H/m). ε_o is generally a tensor quantity but assumed to be a constant scalar quantity (8.85×10^{-12} F/m). $\sigma(\mathbf{r})$ is also assumed to be a scalar quantity, and $\hat{i}$ indicates the imaginary unit.

By combining Eq. (7) with Eq. (8), we have the electric-field full-wave equation,

$$\frac{1}{\mu_o} \nabla \times \nabla \times \mathbf{e}(\mathbf{r}) - \varepsilon_o \omega^2 \mathbf{e}(\mathbf{r}) + \hat{i}\omega \sigma \mathbf{e}(\mathbf{r}) + \hat{i}\omega \mathbf{J}_s(\mathbf{r}) = 0. \tag{11}$$

Eq. (11) is modified to the electric-field diffusion equation by neglecting its second term. In doing this, we have:

$$\frac{1}{\mu_o} \nabla \times \nabla \times \mathbf{e}(\mathbf{r}) + \hat{i}\omega \sigma \mathbf{e}(\mathbf{r}) + \hat{i}\omega \mathbf{J}_s(\mathbf{r}) = 0. \tag{12}$$

Then, we consider the finite-element (FE) formulation (Um et al., 2013) for solving the electric-field diffusion equation. The FE formulation of Eq. (12) starts with its equivalent weak statement. The development of the weak statement requires the multiplication of Eq. (6) by the edge-basis function (Nédélec, 1980) and the integration over the model domain of **V**, resulting in

$$\iiint_{V^e} \mathbf{n}_i^e(\mathbf{r}) \cdot \left(\frac{1}{\mu_o} \nabla \times \nabla \times \mathbf{e}^e(\mathbf{r}) + \hat{i}\omega \sigma^e \mathbf{e}^e(\mathbf{r}) + \hat{i}\omega \mathbf{J}_s(\mathbf{r}) \right) dV = 0, \tag{13}$$

where we use the first-order edge basis functions and tetrahedral elements. The superscript e denotes the eth tetrahedral element, $\mathbf{n}_i^e(\mathbf{r})$, with i varying from 1 to 6 is a set of edge-basis functions, and V^e is the volume of the eth tetrahedral element.

The set of $\mathbf{n}_i^e(\mathbf{r})$ used in Eq. (7) is also chosen as the basis set. Thus, the electric field at a point inside or on a given element is expanded as

$$\mathbf{e}^k(\mathbf{r}) = \sum_{j=1}^{6} \mathbf{e}_j^k(\mathbf{r}) = \sum_{j=1}^{6} u_j^k \mathbf{n}_j^k(\mathbf{r}), \tag{14}$$

where u_j^k is the unknown amplitude of the electric field on edge j of the k^{th} element.

Substituting Eq. (14) into Eq. (13), and using vector calculus identities with the homogeneous Dirichlet boundary conditions, yields

$$(\mathbf{A}^e + \mu_o \omega i \hat{\mathbf{B}}^e)\mathbf{u}^e = -\mu \omega \hat{i} \mathbf{s}^e, \tag{15}$$

where

$$\text{the } (i,j)^{\text{th}} \text{ element of } \mathbf{A}^e = \iiint_{V^e} \nabla \times \mathbf{n}_i^e(\mathbf{r}) \cdot \nabla \times \mathbf{n}_j^e(\mathbf{r}) dV, \tag{16}$$

$$\text{the } (i,j)^{\text{th}} \text{ element of } \mathbf{B}^e = \iiint_{V^e} \mathbf{n}_i^e(\mathbf{r}) \cdot \sigma^e \mathbf{n}_j^e(\mathbf{r}) dV \,, \tag{17}$$

$$\text{the } i^{\text{th}} \text{ element of } \mathbf{s}^e = \iiint_{V^e} \mathbf{n}_i^e(\mathbf{r}) \cdot \mathbf{J}_s(\mathbf{r}) dV \,, \tag{18}$$

$$\mathbf{u}^e = [u_1^e \quad u_2^e \quad \ldots \quad u_6^e] \tag{19}$$

Eq. 15 is considered local, because it results from integration over each individual element. Based on connectivity information about elements in $\mathbf{V}$, the local systems of FE equations derived from the individual elements are assembled into a single global system of equations. Then, the superscript *e* is dropped. The solution of the global version of Eq. (15) determines the electric fields in **V**. Magnetic fields are interpolated from the electric fields using Faraday's law. The system matrix of Eq. (15) is unstructured, sparse, complex, and symmetric. Eq. (15) can be solved using an LU decomposition (Golub and Van Loan, 1996) or quasi-minimal residual method (Freund, 1992) along with an incomplete LU preconditioner (Saad, 2003).

Electrical conductivity models

Once a set of reservoir parameters (e.g., pore fluid saturation S_w, and electrical conductivity of pore fluid σ_w) are determined from coupled flow-geomechanical simulation, the bulk electrical conductivity (σ) of a shaly reservoir can be estimated by Waxman-Smits equation (Waxman and Smits, 1968; Mavko et al., 2009; Kwon and Snieder, 2011):

$$\sigma = \Phi^m S_w^n \left[\sigma_w + BQ_v S_w^{-1} \right], \tag{20}$$

$$\mathrm{B} = 4.78 \times 10^{-8} [1 - 0.6 e^{-\frac{\sigma_w}{0.0013}}] \,, \tag{21}$$

$$\mathrm{Q}_v = \rho_g (1 - \Phi) \Phi^{-1} CEC. \tag{22}$$

In this study, the rock physics parameters of Eqs. (20), (21), and (22) are empirically chosen; both the cementation (*m*) factor and the saturation (*n*) factor are set to 2; the grain density (ρ_g) is set to 2,370 (kg/m^3); the cation exchange capacity (CEC) is set to 38,000 (Coulomb/kg); the electrical conductivity of the pore fluid is set to 3.33 (S/m). Thus, Eq. (20) transforms the reservoir parameters to electrical conductivity values.

Hydraulic fracturing operations force fluids into the formation under high pressure, producing highly localized changes in porosity and pore fluids. Because EM geophysical methods are sensitive to the porosity, fluid saturation, and chemistry of the fluid in the pore space, they are a promising tool for illuminating injected-fluid migration pathways.

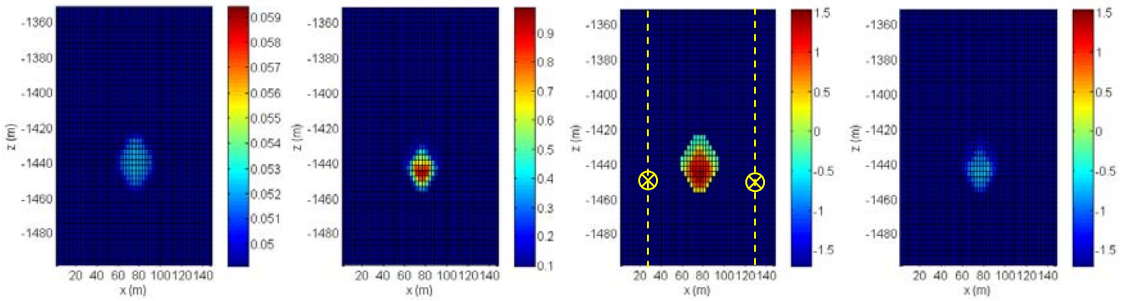

(a) 200 seconds after hydraulic fracturing starts.

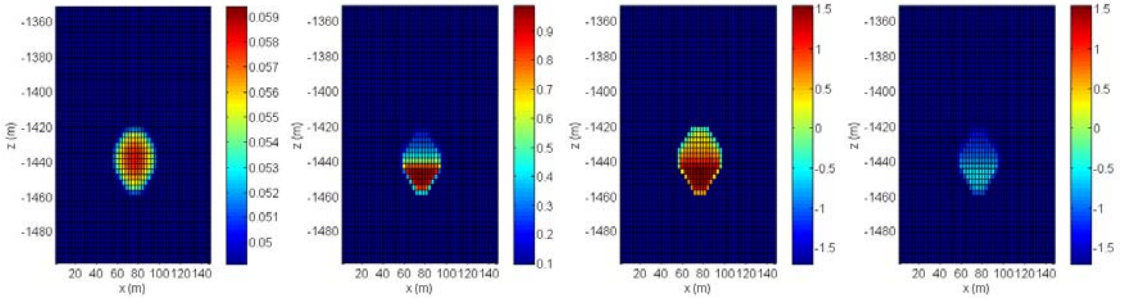

(b) 500 seconds.

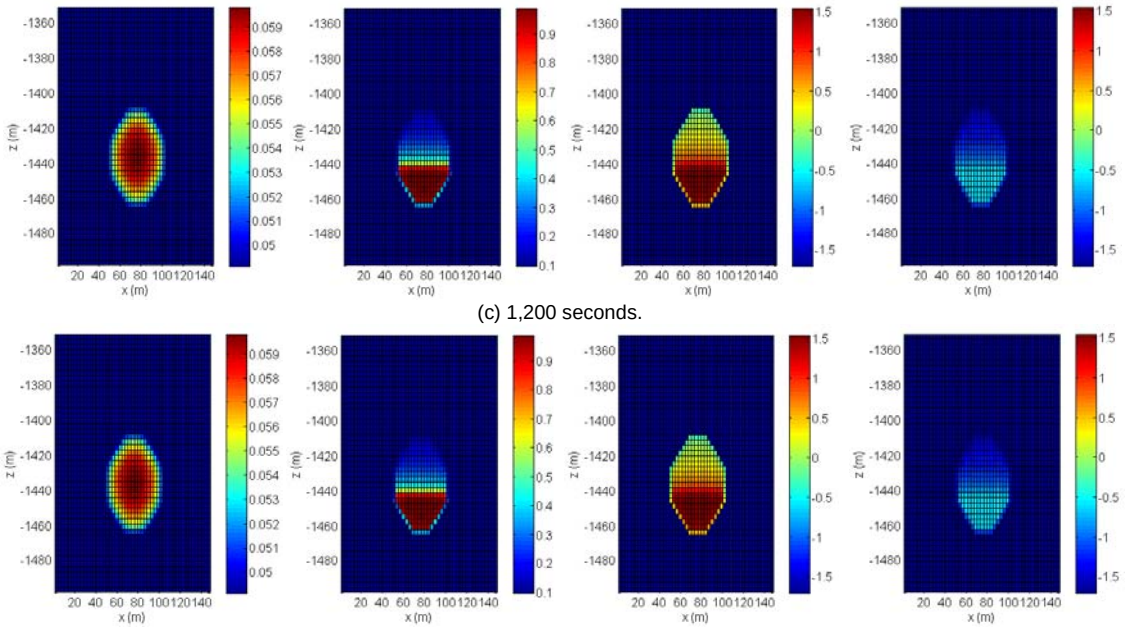

(c) 1,200 seconds.

(d) 1,600 seconds.

Fig. 11 Cross-sectional view (*x-z* plane at the first y layer, stimulated zone) of reservoir models and resultant electrical conductivity models. The 1st column and the 2nd column show changes in porosity and fluid saturation values over time, respectively. The 3rd column shows changes in conductivity values when the electrically-engineered high-conductivity fluid (10,000 S/m) is injected. The 4th column shows changes in conductivity values when the brine (3.33 S/m) is injected. At the top of the third column, the yellow vertical line segments indicate observation wells for the vertical crosswell EM configuration. Two yellow ⊗ indicates the positions of horizontal wells for the horizontal crosswell EM configuration. The color charts for the 1st and 2nd column are linear and those for the 3rd and 4th column are based on the common log.

One primary goal of our EM modeling analysis is to examine the capabilities of an EM geophysical method for sensing bulk conductivity changes that are directly related to migration pathways of injected fluids. For successful EM detection of fluid movement, it is important to ensure a sufficient contrast in electrical conductivity between the intact and stimulated zones. This sufficient contrast can be realized by injecting the brine (3.3 S/m). We can also consider electromagnetically engineered injection fluids that have high magnetic permeability and/or conductivity values. For detailed information about the applications of such fluids, the reader is referred to Muramatsu et al., (1992), Borglin et al. (2000), Oldenburg et al. (2000) and Modius et al. (2001). Recently, Natália Saliés (2012) also shows that a mixture of water and electrically-coated proppants can ensure large constrasts in conductivity between the intact and stimulated zones.

Based on the Waxman-Smits equation, we can transform reservoir parameters to realistic electrical conductivity models. Fig. 11 shows cross-sectional views of reservoir parameters (the first column for reservoir porosity, the second column for fluid saturation, and the third column for electrical conductivity after hydraulic fracturing starts, along with a high-conductivity fluid (10,000 S/m). In Fig. 11, porosity and saturation are volume-averaged within the stimulated zone. For comparison purposes, we also generate the electrical conductivity models (the fourth column) when the brine (3.33 S/m) is injected. As the hydraulic fracturing operation continues, perturbations in porosity and saturation gradually increase in all directions (e.g., leak-off of water).

Note that because fracture propagation is not the same as injected fluid movement, the anomalous conductivity distribution gradually deviates over time from the anomalous porosity distribution, and increasingly resembles the anomalous saturation distribution. Accordingly, EM responses to the given conductivity models will be more directly correlated with the migration pathways of the injected fluids, but might be marginally sensitive to unsaturated fractures. Therefore, when EM geophysical methods are used to characterize hydraulically induced fractures, one should be aware of the possibility that the unsaturated fractures may not be imaged. In contrast, as mentioned earlier, microseismic methods are based on seismic events associated with fracturing, but are insensitive to saturation changes at late times. Therefore, we can expect that the joint analysis of microseismic and EM data would significantly reduce the ambiguity involved in characterizing hydraulically induced fractures. Also note that the use of high-conductivity fluid does not change the overall geometry of anomalous conductivity distribution (compare the third column of Fig. 11 with the fourth column), but significantly increases the conductivity contrast over time. Thus, as will be demonstrated in the next section, its use makes EM geophysical methods more suitable for monitoring migration pathways of the injected fluids.

Crosswell EM methods

As a possible option for monitoring the migration pathways of injected fluids, we consider crosswell EM methods. Crosswell EM methods (Fig. 12) interrogate electrical conductivity structures between wells and can yield detailed 2D/3D

images. These EM methods typically employ solenoids as a transmitter (a wire coil carrying alternating currents). The emitted magnetic source fields are called primary magnetic fields (B_o) and induce currents in nearby formations. In turn, the induced currents generate secondary magnetic fields. The primary and secondary magnetic fields are measured in the other well with magnetic receivers. After a number of sources are excited at different positions in one well, and the magnetic fields are measured at a number of receiver positions in the other well, the conductivity structures between the wells are imaged through inverse modeling. (For details of the crosswell EM methods and their applications, the reader is referred to Alumbaugh and Morrison (1995), Wilt et al. (1995), Zeng et al. (2000), and Gao et al. (2008).) To successfully sense and monitor injection-fluid migration pathways, conductivity changes caused by migration should produce measurable perturbation in the magnetic fields.

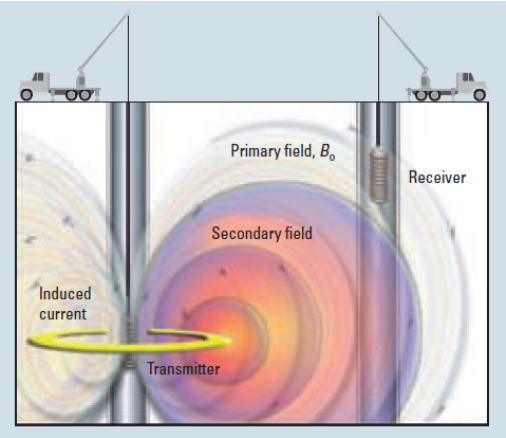

Fig. 12 A typical crosswell EM survey configuration (Courtesy from Schlumberger, 2006). Sources and receivers are lowered into the wells. The primary magnetic fields of the transmitter coil induce the electrical current (yellow). The current produces the secondary magnetic fields (pink). The receivers record the both primary and magnetic fields.

We consider vertical and horizontal crosswell EM configurations—the proposed configurations are shown in Fig. 11(a). The vertical crosswell EM configuration would work well for sensing the height and width of fractures between wells; the horizontal crosswell EM configuration would be sensitive to the thickness of the fractures. For both crosswell EM configurations, well spacing is set to 100 m. The source frequency is set to 3,000 Hz. To allow for the high frequency source in a well environment, it is required that part of the casing in which the sources and receivers are placed is composed of nonmetallic materials (e.g., fiberglass). It is also assumed that magnetic receivers can detect a 1% difference in the magnetic field amplitude, and the receiver noise level is 1.0^{-10} (Ampere/m).

The proposed crosswell EM configurations were simulated using the 3D FE electromagnetic simulator over the electrical conductivity models shown in Fig. 11. Vertical crosswell EM responses to the conductivity models with the high-conductivity fluid and the brine are shown at selected source positions in Figs. 13 and 14, respectively. Horizontal crosswell EM responses to the conductivity models using high-conductivity fluid and the brine are shown in Figs. 15 and 16, respectively. For simplicity, the total magnetic fields and their relative difference with respect to the magnetic fields of 0.02 S/m half-space (i.e., the background conductivity before the injection) are plotted. First, note that all magnetic fields (the left column of Figs. 13 through 16) are above the noise level prescribed above. As the fracture grows larger, both horizontal and vertical crosswell measurements start to sense the fracture. When the brine is injected, the perturbation in the magnetic field is marginal (Figs. 14 and 16). However, this does not imply that the brine is an ineffective tracer when the crosswell EM method is employed to map saturated fractures. In fact, the brine movements have been successfully detected in many enhanced oil recovery operations. However, in this particular case, the brine injection produces few changes in conductivity (the fourth column of Fig. 11), due to the limited increase in porosity (from 0.049 to 0.059) during hydraulic fracturing, resulting in marginal perturbation of the magnetic field. In contrast, Figs. 13 and 15 show that the use of high-conductivity fluid significantly improves (to about an order of magnitude) the sensitivity of crosswell EM measurements to conductivity changes due to hydraulic fracturing operations. We conclude that along with an electromagnetically engineered fluid, the crosswell EM method can serve as an effective mapping tool for conductivity changes directly related to the migration pathways of the injected fluid.

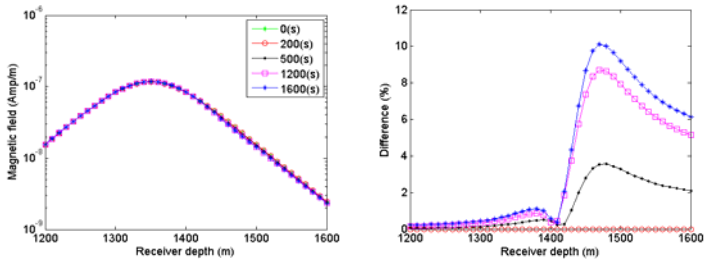

(a) Source at (x=30 m, y=0 m and z=-1350 m).

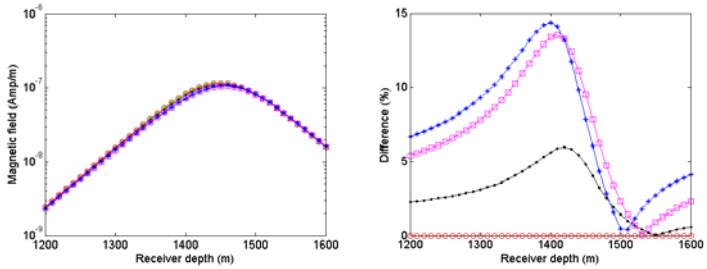

(b) Source at (x=30 m, y=0 m and z=-1450 m).

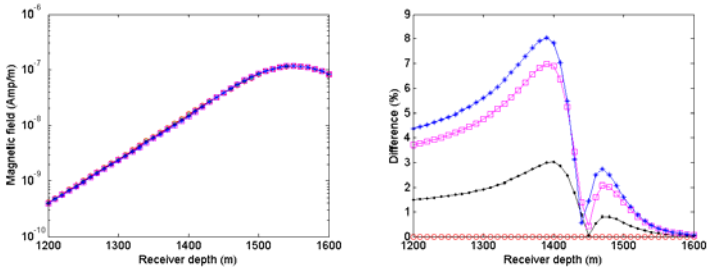

(c) Source at (x=30 m, y=0 m and z=-1550 m).

Fig. 13 Magnetic field amplitudes (the left column) and their relative difference (the right column) with respect to the background magnetic field when the vertical crosswell configuration is applied to the conductivity model shown in the third column of Fig. 11. Receivers are placed along the axis that is parallel to the z-axis and passes through the point (x=130 m and y=0 m).

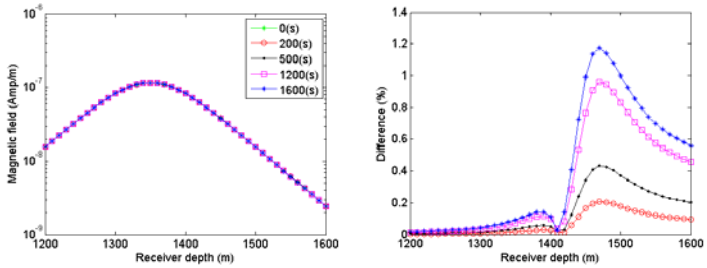

(a) Source at (x=30 m, y=0 m and z=-1350 m).

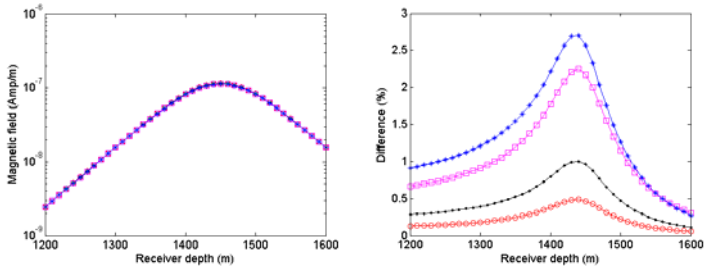

(b) Source at (x=30 m, y=0 m and z=-1450 m).

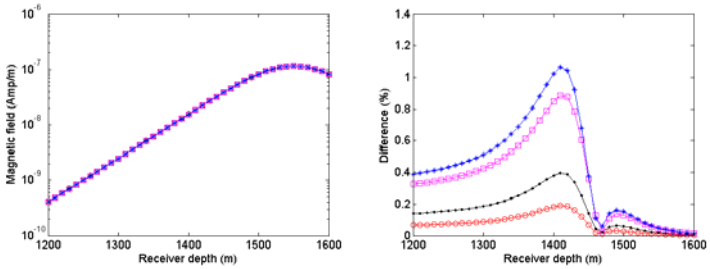

(c) Source at (x=30 m, y=0 m and z=-1550 m).

Fig. 14 Magnetic field amplitudes (the left column) and their relative difference (the right column) with respect to the background magnetic field when the vertical crosswell configuration is applied to the conductivity model shown in the fourth column of Fig. 11. Receivers are placed along the axis that is parallel to the z-axis and passes through the point (x=130 m and y=0 m).

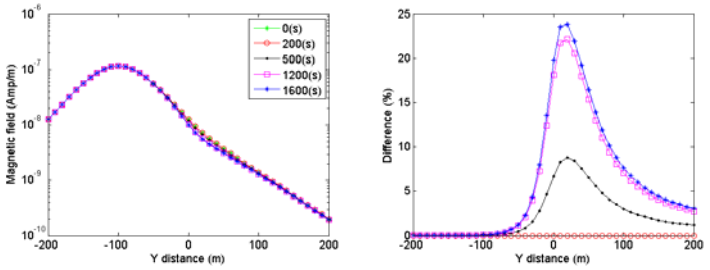

(a) Source at (x=30 m, y=-100 m and z=-1440 m).

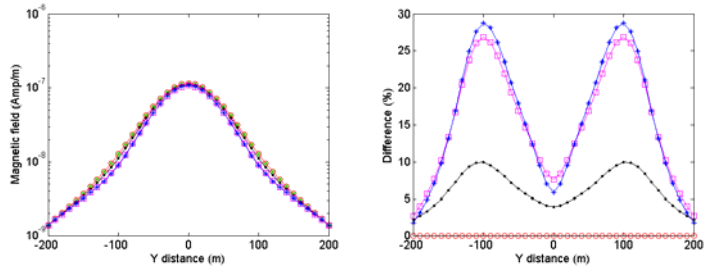

(b) Source at (x=30 m, y=0 m and z=-1440 m).

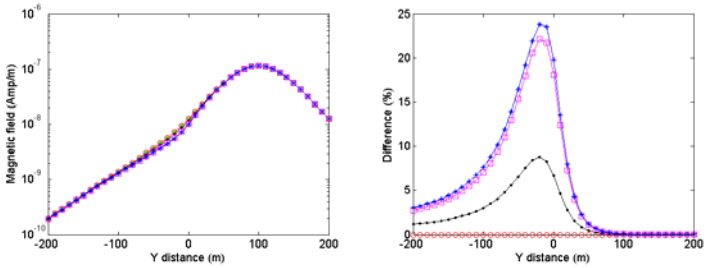

(c) Source at (x=30 m, y=100 m and z=-1440 m).

Fig. 15 Magnetic field amplitudes (the left column) and their relative difference (the right column) with respect to the background magnetic field when the horizontal crosswell configuration is applied to the conductivity model shown in the third column of Fig. 11. Receivers are placed along the axis that is parallel to the y-axis and passes through the point (x=130 m and z=-1440 m).

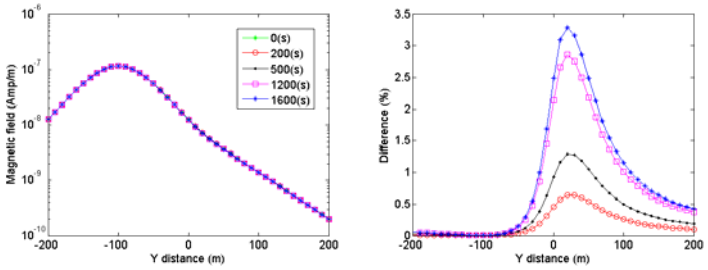

(a) Source at (x=30 m, y=-100 m and z=-1440 m).

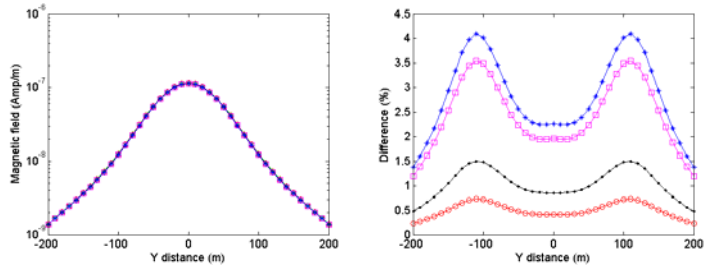

(b) Source at (x=30 m, y=0 m and z=-1440 m).

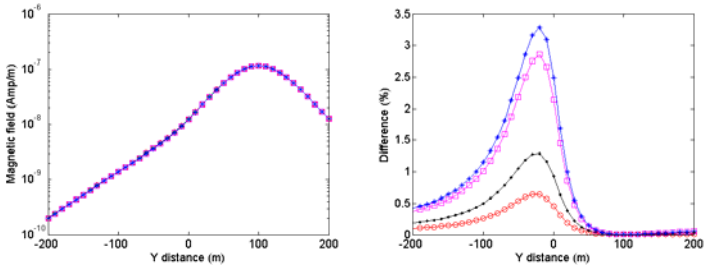

(c) Source at (x=30 m, y=100 m and z=-1440 m).

Fig. 16 Magnetic field amplitudes (the left column) and their relative difference (the right column) with respect to the background magnetic field when the horizontal crosswell configuration is applied to the conductivity model shown in the fourth column of Fig. 11. Receivers are placed along the axis that is parallel to the y-axis and passes through the point (x=130 m and z=-1440 m).

Conclusions

During hydraulic fracturing operations, we investigated geomechanical and flow responses induced by water injection. From the numerical results, we found that fracture propagation is not the same as propagation of the water front. The gap between the water front and the fracture top is more dominant at later times, after a large amount of water has been injected and that gap is filled with reservoir gas. We also found considerable leak-off of water to the reservoir. The inconsistency between the fracture volume and the volume of injected water could lead to underestimating the fracture propagation, if we were to make the simple assumption that the fracture is fully saturated with injected water. We identified fluctuation in pressure and displacement under constant water injection. As the fracture dimension becomes larger, the fluctuation decreases. All the complex physical processes above are fundamentally based on tight coupling between flow and geomechanics, which have different time scales between them.

Owing to the rigorous 3D modeling capabilities of a recently developed coupled flow-geomechanical simulator, T+M, we have been able to generate a series of realistic electrical conductivity models that reveals transient changes in conductivity within shaly reservoirs during hydraulic fracturing operations. Because the injected fluid movement is separated from the fracture propagation at late times, conductivity models are more closely related with the migration pathways of injected fluids rather than unsaturated fractures. The 3D FE Maxwell's equations solver was used in this study to simulate crosswell EM methods over a series of conductivity models. Our modeling analysis suggests that the crosswell EM method can serve as an effective mapping tool for conductivity changes along the migration pathways of the injected fluids. Since our sensitivity analysis demonstrates sufficient perturbation in the magnetic fields during hydraulic fracturing, we expect that 3D inverse modeling of the crosswell EM measurements will be able to determine spatial distribution of electrical conductivity around the wells, and make it possible to delineate fluid-migration pathways and fracture geometry. The resulting conductivity images will also provide a clearer understanding of the fractured reservoir. Further sensitivity analyses—with different types of electromagnetically engineered fluids and proppants, optimal geophysical survey designs (both borehole-based and surface-based) for typical hydraulic fracturing scenarios and subsequent geophysical imaging experiments—will be conducted in our future research.

Acknowledgement

This study was supported by the US Environmental Protection Agency, Office of Water, under an Interagency Agreement with the U.S. Department of Energy at the Lawrence Berkeley National Laboratory through Contract No. DE-AC02-05CH11231, and by RPSEA (Contract No. 08122-45) through the Ultra-Deepwater and Unconventional Natural Gas and Other Petroleum Resources Research and Development Program as authorized by the US Energy Policy Act (EPAct) of 2005. The research described in this article has been funded wholly (or in part) by the U.S. Environmental Protection Agency through Interagency Agreement (DW-89-92235901-C) to the Lawrence Berkeley National Laboratory. The views expressed in this article are those of the author(s) and do not necessarily reflect the views or policies of the EPA.

References

Adachi, J., Siebrits, E., Peirce,A., Desroches, J., 2007. Computer simulation of hydraulic fractures. *Int. J. Rock. Mech. Min.* , **44**,739–757.

Alumbaugh, D., Morrison, H.F. 1995. Monitoring subsurface changes over time with cross well electromagnetic tomography. *Geophysical Prospecting* **43**: 873-902.

Asahina D., Landis E.N., Bolander J.E. 2011. Modeling of phase interfaces during pre-critical crack growth in concrete. *Cement and Concrete Composites* **33**: 966–977.

Berryman JG. 2002 Extension of poroelastic analysis to double-porosity materials: New technique in microgeomechanics. *J. Eng. Mech.* ASCE; **128**(8):840 – 847.

Borglin, S.E., G.J. Moridis, C.M. Oldenburg, 2000, Experimental Studies of the Flow of Ferrofluids in Porous Media, *Transport in Porous Media*, **41**: 61-80.

Cipolla C.L., Lolon E.P., Erdle J.C., Rubin. B., 2010 Reservoir modeling in shale-gas reservoirs. *SPE Reserv. Eval. Eng.* 638–653.

Coussy, O., 2004 Poromechanics. Chichester, England: John Wiley and Sons.

Dean, R.H. and Schmidt, J.H., 2008 Hydraulic fracture predictions with a fully coupled geomechanical reservoir simulation. *SPEJ*, **14**(4):707-714

Fisher K. and Warpinski N 2012 Hydraulic fracture-height growth: real data. *SPE Prod. Oper.* **27**(1):8-19

Fjaer, E., Holt, R.M., Horsrud, P., Raaen, A.M., Risnes, R., 2008. *Petroleum related rock mechanics*, 2nd ed. Elsevier B.V., Amsterdam,T he Netherlands.

Freund, R., 1992, Conjugate gradient type methods for linear systems with complex symmetric coefficient matrices, SIAM *Journal Scientific Statistical Computing*, **13**:425-448.

Gao G., D. Alumbaugh, P. Zhang, H. Zhang, C. Levesque, R. Rosthal, J. Liu, A. Abubakar, and T. Habashy, 2008, Practical Implications of Nonlinear Inversion For Cross-well Electromagnetic Data Collected In Cased-wells, SEG Annual Meeting Abstract.

Golub G. H. and C.F. Van Loan, 1996, Matrix computation, 3rd edition: Johns Hopkins University Press.

Ji, L., and Settari A., and Sullivan, R.B. 2009 A novel hydraulic fracturing model fully coupled with geomechanics and reservoir simulation. *SPEJ*..423-430.

Johnson, R. and J. Shrallow, 2011, Ambiguity in microseismic monitoring, SEG Annual Meeting Abstract.

Kargbo, D.M., Wilhelm, R.G., Campbell, D.J., 2010 Natural gas plays in the Marcellus shale: Challenges and potential opportunities. *Environ. Sci. Technol.*,**44**(5):5679–5684.

Kim J., Sonnenthal E., and Rutqvist J. 2012 Formulation and sequential numerical algorithms of coupled fluid/heat flow and geomechanics for multiple porosity materials. *Int. J. Numer. Meth. Engrg.* **92**:425-456, doi: 10.1002/nme.4340.

Kim J, and Moridis G.J. 2013 Development of the T+M coupled flow-geomechanical simulator to describe fracture propagation and coupled flow-thermal-geomechanical processes in tight/shale gas systems. *Comput. Geosci.* **60**:184-198.

King, G. E., 2012 Hydraulic fracturing 101: What every representative, environmentalist, regulator, reporter, investor, university researcher, neighbor and engineer should know about estimating frac risk and improving frac performance in unconventional gas and oil wells. SPE Hydraulic Fracturing Technology Conference, The woodland, TX, Feb. 6-8. 2012.

Kwon, Myong Jae and Roel Snieder, 2011, Uncertainty analysis for the integration of seismic and controlled source electromagnetic data, Geophysical Prospecting, 59, 609-626.

Moridis, G. J., C. M. Oldenburg, 2001, Process for guidance, containment, treatment, and imaging a subsurface environment utilizing ferro-fluids, United Satates Patent, Patent No., US6250848B1.

Moridis, G.J., Kowalsky, M.B., Pruess, K., 2008 Tough+hydrate v1.0 user's manual: A code for the simulation of system behavior in hydrate-bearing geologic media. In: Report LBNL-00149E. Lawrence Berkeley National Laboratory, Berkeley, CA.

Muramatsu, S., S. Takasugi, K. Osato, 1992, Three-dimensional detection system for detecting fractures and their distributions in the earth crust utilizing an artificial magnetic field and magnetic particle tracer, United States Patent, Patent No., 5151658.

Nédélec, J.-C., 1980, Mixed finite elements in R3: *Numerische Mathematik*, **35**:315–341.

Nordren,R.P.,1972. Propagation of a vertical hydraulic fracture. *SPEJ*. **12**(8), 306–314,SPE7834.

Oldenburg, C., S.E. Borglin, and G. J. Moridis, 2000, Numerical Simulation of Ferrofluid Flow for Subsurface Environmental Applications, *Transport in Porous Media*, **38**:319-344.

Osborn, S.G., Vengosh, A., Warner, N.R., Jackson, R.B., 2011, Methane contamination of drinking water accompanying gas-well drilling and hydraulic fracturing. *PNAS*,**108**:8172–8176.

Page, J.C., Miskimins, J.L., 2009, A comparison of hydraulic and propellant fracture propagation in a shale gas reservoir. J. Can. Petrol. Technol., **48**(5):26–30.

Perkins, T.K., Kern, L.R., 1961, Widths of hydraulic fractures. JPT **13**(9), 937–949, SPE89.

Ribeiro, L. H., Sarma, M. M., 2013 Fluid selection for energized fracture treatments. SPE Hydraulic Fracturing Technology Conference, The woodland, TX, Feb. 4-6. 2013.

Ruiz, G., Ortiz, M., Pandolfi, A., 2000, Three-dimensional finite-element simulation of the dynamic Brazilian tests on concrete cylinders. *Int. J. Numer. Meth. Engrg*. **48**,963–994.

Rutqvist, J., Rinaldi, A.P., Cappa, F., Moridis G.J., 2013, Modeling of fault reactivation and induced seismicity during hydraulic fracturing of shale-gas reservoirs., *J. Pet. Sci. Eng*. **107**:31-44

Rutqvist, J., Stephansson, O.. 2003, The role of hydromechanical coupling in fractured rock engineering. Hydrogeol. J,. **11**:7–40.

Saad, Y., 2003, Iterative methods for sparse linear systems, SIAM.

Saliés, Natália Gastão, 2012, Study on the feasibility of using electromagnetic methods for fracture diagnostics, Thesis of Master of Science in Engineering, University of Texas at Austin.

Schlumberger, 2006, Middle East and Asia Reservoir Review, 24-32

Snow, D.T., 1965, A parallel plate model of fractured permeable media., Ph.D thesis, University of California, Berkeley.

Tzchichholz, F., Herrmann, H. J., 1995, Simulations of pressure fluctuations and acoustic emission in hydraulic fracturing. *Phys. Rev. E*, **51**(3):1961-1970.

Um, E., M. Commer, G. Newman, 2013, Efficient pre-conditioned iterative solution strategies for the electromagnetic diffusion in the Earth: finite-element frequency-domain approach, *Geophysical Journal International*, **193**:1460-1473.

van Genuchten, 1980, A closed-form equation for predicting the hydraulic conductivity of unsaturated soils. Soil Sci. Soc. Am, J., (44):892–898.

Vermylen J.P and Zoback M.D. 2011 Hydraulic fracturing, microseismic magnitudes, and stress evolution in the Barnett Shale. USA. Hydr. Frac. Tech. Conf. The woodland, TX, 24 – 26 Jan.

Warpinski, N. R., Kramm, R. C., Heinze, J. R., Waltman, C. K., 2005, Comparison of single- and dual-array microseismic mapping techniques in the Barnett shale. SPE ATCE, Dallas, Oct. 9-12. 2005. SPE95568

Waxman, M. H. and Smits, L. J. M., 1968, Electrical conductivities in oil-bearing shaly sands, *SPEJ* **8**:107-122.

Wilt, M., Alumbaugh, D., Morrison, H.F., Becker, A., Lee, K.H., Deszcz-Pan, M. 1995, Crosshole electromagnetic tomography: System design considerations and field results. *Geophysics* **60**: 871-885.

Witherspoon, P.A., Wang, J.S.Y., Iwai, K., Gale, J.E., 1980, Validity of cubic law for fluid flow in a deformable rock fracture. *Water. Resour. Res.* **16**(6):1016–1024.

Zang, A., Stephansson, O., 2010, Stress field of the Earth's crust. Springer Science+Business Media B.V.

Zeng, W., Zhao, W., Wilt, M. 2000. Three Successful Large-scale Field Tests of Crosshole Electromagnetic Tomography Technology. Paper SPE 63143.

Zoback, M., Kitasei, S., Copithorne, B.. 2010 Addressing the environmental risks from shale gas development. Worldwatch Institute Briefing Paper 1 (Worldwatch Inst,W ashington DC).

Zoback M.D. 2007 *Reservoir geomechanics.* Cambridge, Cambridge university press.